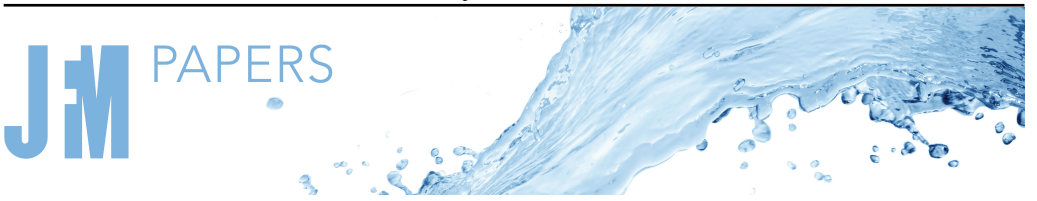
J. Fluid Mech. (2025), *vol.* 1016, A27, doi:10.1017/jfm.2025.10354



Single-mode Rayleigh–Taylor instability in time-dependent rarefaction-driven flows

Yue Li[1], **Xing Gao**[1], **Xu Guo**[1], **Zhigang Zhai**[1] **and Xisheng Luo**[1,2]

[1]Department of Modern Mechanics, University of Science and Technology of China, Hefei 230026, PR China

[2]State Key Laboratory of High-Temperature Gas Dynamics, Institute of Mechanics, Chinese Academy of Sciences, Beijing 100190, PR China

Corresponding authors: Zhigang Zhai, sanjing@ustc.edu.cn; Xu Guo, clguoxu@ustc.edu.cn

(Received 24 February 2025; revised 10 May 2025; accepted 10 June 2025)

Rayleigh–Taylor instability (RTI) caused by rarefaction waves not only features variable acceleration but also incorporates time-dependent density, which introduces great challenges in predicting the finger growth behaviours. In this work, we propose a model for predicting the single-mode finger behaviours by extending the Layzer potential-flow framework to account for time-dependent acceleration and density. Relative to the previous models, the present model can evaluate the effect of time-dependent density on finger growth, and can describe the growth behaviours of both bubbles and spikes in rarefaction-driven RTI flows. In addition, the time-dependent curvature of the finger tip as it evolves from its initial value to the quasi-steady value is quantified. To validate the model, rarefaction-tube experiments and numerical simulations are conducted across a wide range of initial conditions. The results show that the present model can accurately capture the amplitude growth and curvature evolution of bubbles and spikes across various density ratios. Moreover, both the present model and experiments demonstrate that the continuous density reduction in rarefaction-driven flows causes larger asymptotic velocities of bubbles and spikes, leading to higher Froude numbers relative to those under constant or time-dependent acceleration.

Key words: gas dynamics

1. Introduction

When a perturbed interface separating two fluids of different densities is continuously accelerated from the light fluid towards the heavy one, Rayleigh–Taylor instability (RTI) occurs (Rayleigh 1883; Taylor 1950). This instability is driven by baroclinic vorticity arising from the misalignment of the pressure gradient and the local density gradient.

© The Author(s), 2025. Published by Cambridge University Press.

https://doi.org/10.1017/jfm.2025.10354 Published online by Cambridge University Press

Initially, perturbation growth enters a linear stage with an exponential growth rate. Then, in the nonlinear stage, large-scale finger structures of bubbles (light fluids penetrating into heavy fluids) and spikes (heavy fluids intruding into light fluids) emerge. The finger growth in this stage first follows an approximately constant rate, known as the quasi-steady stage, before potentially undergoing re-acceleration (Ramaprabhu *et al.* 2006). Over time, these finger structures evolve across a wide range of scales, eventually transitioning to turbulence.

The RTI can be induced by various factors, most commonly by gravity. A typical occurrence in gravitational fields is the destabilisation of the interface when a heavy fluid is placed above a light fluid. Since the pioneering work of Rayleigh (1883) and the modern development by Taylor (1950), RTI under constant acceleration has been extensively investigated. Theoretically, several nonlinear models extended from the Layzer potential-flow framework (Layzer 1955) have been established to characterise the finger evolution during the quasi-steady stage (Hecht, Alon & Shvarts 1994; Alon *et al.* 1995; Mikaelian 1998; Zhang 1998; Goncharov 2002; Abarzhi 2003; Sohn 2003; Zhang & Guo 2016; Guo & Zhang 2020; Liu *et al.* 2023*a*,*b*). Numerical studies have validated the asymptotic finger behaviour predicted by these nonlinear models (Ramaprabhu & Dimonte 2005; Zhou, Zhang & Tian 2018), and a re-acceleration of the finger growth beyond the quasi-steady stage was observed (Ramaprabhu *et al.* 2006; Wei & Livescu 2012; Bian *et al.* 2020; Fu *et al.* 2023). The self-similar evolution of fingers in the turbulent mixing stage has been numerically investigated, with particular attention to the dependence of late-time mixing on initial conditions (Dimonte *et al.* 2004; Ramaprabhu, Dimonte & Andrews 2005; Cabot & Cook 2006; Youngs 2013). Experimentally, RTI has been explored in water and gas channels (Snider & Andrews 1994; Banerjee & Andrews 2006; Andrews & Dalziel 2010; Banerjee, Kraft & Andrews 2010; Akula *et al.* 2017) and in stationary tanks with a sliding plate separating two fluids (Linden, Redondo & Youngs 1994; Jacobs & Dalziel 2005; Lawrie & Dalziel 2011). In these experiments, an initially random perturbation was typically introduced to investigate the development of large- and small-scale structures in the turbulent mixing stage. In addition, the magnetic levitation technique (Pacitto *et al.* 2000; Huang *et al.* 2007; White *et al.* 2010) and the soap-film technique (Liang *et al.* 2024) have been employed to maintain a heavy fluid on top of a light one. These techniques allow for the creation of single-mode perturbations, enabling detailed examination of instability development across both linear and nonlinear regimes.

The RTI driven by time-dependent acceleration has been experimentally studied using gas guns (Kucherenko *et al.* 1997, 2003), rocket rigs (Read 1984; Youngs 1989) or linear electric motors (Dimonte *et al.* 1996; Dimonte & Schneider 2000), with acceleration varying from tens to hundreds of times the gravitational acceleration. Random multi-mode perturbations were produced in these experiments to explore the RTI-induced turbulence. In contrast, single-mode perturbations were formed in drop tower experiments with low acceleration variations (0.33–1.35 times gravitational acceleration), and a detailed analysis of finger growth in the linear and nonlinear stages was conducted (Waddell, Niederhaus & Jacobs 2001; Wilkinson & Jacobs 2007). Analytical models applicable to finger amplitudes and mixing layer widths across linear, nonlinear and turbulent regimes were developed by Mikaelian (2014), who extended the potential-flow model of Layzer (1955) to flows governed by time-dependent acceleration. Additionally, Ramaprabhu *et al.* (2016) derived two models for variable acceleration scenarios, with one based on the Layzer potential-flow framework for two-dimensional (2-D) bubbles, and the other employing a drag–buoyancy approach for both bubbles and spikes in two and three dimensions. The predictions from both models of Ramaprabhu *et al.* (2016) agreed well with the numerical counterparts under various time-dependent acceleration histories.

https://doi.org/10.1017/jfm.2025.10354 Published online by Cambridge University Press

Differing from the RTI driven solely by constant or variable acceleration, rarefaction-driven RTI not only features variable acceleration but also incorporates time-dependent density (Gao *et al.* 2024), since the pressure in rarefaction regions decreases from the rarefaction head to the tail. In recent decades, rarefaction-driven RTI has received increasing attention due to its critical relevance in inertial confinement fusion (ICF) and air-breathing engines (Aglitskiy *et al.* 2010; Zhou 2017*a*,*b*; Urzay 2018; Zhou *et al.* 2019, 2021, 2025). In ICF, the laser-driven shock strikes the ablator/fuel interface, forming rarefaction waves that propagate back toward the ablation front. The interaction between these rarefaction waves and the ablation front leads to RTI-induced perturbation growth, enhancing mixing between the outer ablators and inner fuels, thereby reducing the fusion yield (Goncharov *et al.* 2000; Qiao & Lan 2021). In air-breathing engines, the rarefaction waves generated due to geometric corners or fuel injection create vorticity at the oxidiser/fuel interface, leading to mixing enhancement and thereby improving the propulsion efficiency (Li, Kailasanath & Book 1991; Li & Book 1991). As a result, it is of significance to explore the mechanism of rarefaction-driven RTI.

The pioneering experimental studies on the rarefaction-driven RTI of liquid interfaces were performed by Lewis (1950) in a rectangular tube connected to a large air reservoir. Their experimental results verified the linear stability theory proposed by Taylor (1950). Recently, continuous 2-D and 3-D single-mode gaseous interfaces were produced in a vertical rarefaction tube, and both the early- and late-time RTI finger growth behaviours across various density ratios were investigated (Morgan *et al.* 2016, 2018; Morgan & Jacobs 2020). Theoretically, the model of Layzer (1955) was extended by Mikaelian (2009) to describe the finger growth in flows with time-dependent acceleration and density. Due to the failure of the potential function in characterising the spike growth (Abarzhi 2003; Mikaelian 2008), the model of Mikaelian (2009) was only formulated for bubbles. Numerically, Li *et al.* (1991) and Li & Book (1991) investigated the rarefaction-driven interface evolution in supersonic flows, observing significant mixing enhancement due to sustained rarefaction-induced vorticity deposition. Liang *et al.* (2020) focused on RTI driven by narrow-width rarefaction waves, and found that the rarefaction-induced RTI evolves more quickly than the shock-induced Richtmyer–Meshkov instability. Wang *et al.* (2022*a*,*b*) studied the effects of interface diffusion on the transition to turbulence in rarefaction-driven flows, and found that the transition is delayed as the diffusion thickness increases.

Up to now, most previous models have been developed for describing finger growth under constant or time-dependent acceleration scenarios. Although the model proposed by Mikaelian (2009) addressed the finger growth under the combined effects of variable acceleration and density, it was only constructed for bubbles. Currently, a theoretical framework for characterising the spike growth under time-dependent acceleration and density conditions is still lacking. The previous work has shown that the bubble exhibits different growth behaviours when the density varies with time or not (Goncharov & Li 2005). As a result, it is desirable and significant to construct a theoretical model that can characterise both bubble and spike growth under time-dependent acceleration and density conditions. In addition, experimental studies on rarefaction-driven RTI are still scarce, except for the work of Morgan *et al.* (2016, 2018), who focused on the developments of continuous interfaces created by the gas diffusion technique. The previous work has proven that gas diffusion can potentially influence the perturbation growth (Duff, Harlow & Hirt 1962; Brouillette & Sturtevant 1994; Motl *et al.* 2009; Morgan *et al.* 2018). Therefore, it is desirable to carry out experimental studies on rarefaction-driven RTI with discontinuous interfaces, which motivates the present work.

https://doi.org/10.1017/jfm.2025.10354 Published online by Cambridge University Press

In this study, the finger growth dynamics of 2-D single-mode interfaces driven by rarefaction waves is investigated. In the following, a unified model for both bubbles and spikes at arbitrary density ratios is first developed by extending the potential-flow framework of Layzer (1955) to account for the time-dependent acceleration and density. The model primarily focuses on finger growth up to the quasi-steady stage, consistent with the scope of most previous studies. Then, a series of experiments with discontinuous interfaces and numerical simulations is performed to examine the validity of the model.

2. Theoretical formulation

In 2-D flows where both acceleration and density are time-dependent, two inviscid and irrotational semi-infinite fluids, initially separated by a single-mode perturbation, are considered. Based on the Layzer potential-flow model (Goncharov & Li 2005; Mikaelian 2009), the governing equations for this system can be expressed as

$$\nabla^2\phi_i + \frac{\dot{\rho}_i(t)}{\rho_i(t)} = 0, \tag{2.1}$$

$$\frac{\partial z}{\partial t} + \frac{\partial \phi_i}{\partial x}\frac{\partial z}{\partial x} - \frac{\partial \phi_i}{\partial z} = 0, \tag{2.2}$$

$$\sum_{i=1}^{2}(-1)^i \rho_i(t)\left\{g(t)z + \frac{\partial \phi_i}{\partial t} + \frac{1}{2}\left[\left(\frac{\partial \phi_i}{\partial x}\right)^2 + \left(\frac{\partial \phi_i}{\partial z}\right)^2\right]\right\} = f(t). \tag{2.3}$$

Here, the coordinates x and z are perpendicular and parallel to the time-dependent acceleration $g(t)$, respectively, ϕ_i denotes the velocity potential and $\rho_i(t)$ denotes the fluid density. The subscripts i $(= 1, 2)$ correspond to the two fluids: for bubbles, $i = 1$ refers to the heavy fluid, $i = 2$ to the light fluid and $g(t) > 0$; for spikes, the situation is reversed, with $i = 1$ corresponding to the light fluid, $i = 2$ to the heavy fluid and $g(t) < 0$. This definition can simplify the analysis, enabling a consistent treatment of both bubbles and spikes (Zhang & Guo 2016), and also results in a signed Atwood number A $(= (\rho_1 - \rho_2)/(\rho_1 + \rho_2))$, with $A > 0$ for bubbles, and $A < 0$ for spikes. Following Layzer's approach, the shape of the finger tip is approximated by a parabola, $z(x, t) = \eta(t) + k\xi(t)x^2$, where k denotes the wavenumber of the initial interface, and $\eta(t)$ and $\xi(t)$ denote the finger amplitude and the finger-tip curvature, respectively.

In the governing equations, (2.1) is essentially Laplace's equation for the velocity potential ϕ_i, with an additional term $\dot{\rho}_i(t)/\rho_i(t)$ representing a dilatation effect due to time-dependent density $\rho_i(t)$. Physically, this term acts as an effective body force arising from mass conservation under non-stationary density variations. Equation (2.2) represents the kinematic boundary condition at the interface, which enforces that fluid particles initially on the interface remain there for all time. Equation (2.3) represents the dynamic boundary condition, which imposes pressure continuity across the interface. In (2.3), the term $\rho_i(t)g(t)z$ denotes the potential under time-dependent acceleration, while the remaining terms on the left-hand side correspond to the unsteady Bernoulli contributions for fluid i. The function $f(t)$, an integration constant from pressure matching, is typically set to $f(t) = 0$ by defining a reference pressure datum.

In Layzer's potential-flow framework, the potential function is often represented by a Fourier series, $\phi_i = \sum_{j=1}^{\infty} P_i(t)^{(j)} \cos(jkx)e^{(-1)^i jkz}$. In this series, lower-order terms dominate, while higher-order terms contribute minimally due to their exponential decay with increasing order. Retaining more modes enhances the accuracy of early-time finger behaviour but becomes unsuitable for late-time behaviour because the series diverges at

https://doi.org/10.1017/jfm.2025.10354 Published online by Cambridge University Press

large times (this divergence is especially severe for spikes in high Atwood number cases). In our model, the first term of the Fourier series, denoted as $P_i(t)\cos(kx)e^{(-1)^i kz}$, is used to characterise the dominant behaviour of the finger. Following Zhang & Guo (2016), we approximate the contribution of all remaining terms $\sum_{j=2}^{\infty} P_i(t)^{(j)}\cos(jkx)e^{(-1)^i jkz}$ by $Q_i(t)\cos(c(t)kx)e^{(-1)^i c(t)kz}$, where $c(t)$ is dependent on the density ratio. Finally, the velocity potentials for compressible fluids can be written as

$$\phi_i = P_i(t)\cos(kx)e^{(-1)^i kz} + Q_i(t)\cos(c(t)kx)e^{(-1)^i c(t)kz} - \frac{\dot{\rho}_i(t)}{2\rho_i(t)}z^2, \quad i = 1,\ 2, \tag{2.4}$$

where the term, $\dot{\rho}_i(t)z^2/[2\rho_i(t)]$, denoting a density-related component for compressible fluids, is obtained by the solution of (2.1) expanded up to x^2 (Goncharov & Li 2005); and $P_i(t)$ and $Q_i(t)$, depending on time t, are also functions of A and g.

Substituting (2.4) into (2.2) and expanding the resulting equations through the order of x^2 yields

$$\dot{\eta}(t) - (-1)^i k\left[P_i(t)e^{(-1)^i k\eta(t)} + c(t)Q_i(t)e^{(-1)^i c(t)k\eta(t)}\right] + \frac{\dot{\rho}_i(t)\eta(t)}{\rho_i(t)} = 0, \tag{2.5}$$

$$\begin{aligned} &2\dot{\xi}(t) - 6k^2\xi(t)\left[P_i(t)e^{(-1)^i k\eta(t)} + c(t)^2 Q_i(t)e^{(-1)^i c(t)k\eta(t)}\right] + \\ &(-1)^i k^2\left[P_i(t)e^{(-1)^i k\eta(t)} + c(t)^3 Q_i(t)e^{(-1)^i c(t)k\eta(t)}\right] + \frac{2\dot{\rho}_i(t)\xi(t)}{\rho_i(t)} = 0. \end{aligned} \tag{2.6}$$

By solving $P_i(t)$, $Q_i(t)$ from the above equations and substituting the resulting expressions into (2.3), one can obtain an ordinary differential equation for the term proportional to x^2

$$F_1\frac{\mathrm{d}^2\eta}{\mathrm{d}t^2} + F_2\frac{\mathrm{d}^2\xi}{\mathrm{d}t^2} + F_3\left[k^2c^2\left(\frac{\mathrm{d}\eta}{\mathrm{d}t}\right)^2 + 16\left(\frac{\mathrm{d}\xi}{\mathrm{d}t}\right)^2\right] + F_4\frac{\mathrm{d}\xi}{\mathrm{d}t}\frac{\mathrm{d}c}{\mathrm{d}t} + F_5\frac{\mathrm{d}\xi}{\mathrm{d}t} + F_6\frac{\mathrm{d}c}{\mathrm{d}t} + F_7 = 0, \tag{2.7}$$

where $\mathrm{d}\eta/\mathrm{d}t$ denotes the finger growth rate, and

$$F_1 = 2k\xi(-\rho_1 + \rho_2) - \frac{kc\rho_1}{1 + c + 6\xi} - \frac{kc\rho_2}{1 + c - 6\xi}, \tag{2.8}$$

$$F_2 = \frac{2\rho_1}{1 + c + 6\xi} + \frac{2\rho_2}{1 + c - 6\xi}, \tag{2.9}$$

$$F_3 = \frac{-\rho_1}{(1 + c + 6\xi)^2} + \frac{\rho_2}{(1 + c - 6\xi)^2}, \tag{2.10}$$

$$F_4 = \frac{-2\rho_1}{(1 + c + 6\xi)^2} + \frac{-2\rho_2}{(1 + c - 6\xi)^2}, \tag{2.11}$$

$$F_5 = \frac{10kc\dot{\eta}\rho_1 + 2(1 + c - 4\xi + 5kc\eta)\dot{\rho}_1}{(1 + c + 6\xi)^2} + \frac{-10kc\dot{\eta}\rho_2 + 2(1 + c + 4\xi - 5kc\eta)\dot{\rho}_2}{(1 + c - 6\xi)^2}, \tag{2.12}$$

$$F_6 = \frac{(-1 - 6\xi)k\dot{\eta}\rho_1 - (2\xi + k\eta + 6k\eta\xi)\dot{\rho}_1}{(1 + c + 6\xi)^2} + \frac{(-1 + 6\xi)k\dot{\eta}\rho_2 - (2\xi + k\eta - 6k\eta\xi)\dot{\rho}_2}{(1 + c - 6\xi)^2}, \tag{2.13}$$

https://doi.org/10.1017/jfm.2025.10354 Published online by Cambridge University Press

$$F_7 = -\frac{kc\dot{\eta}\dot{\rho}_1(2kc\eta + c + 2\xi + 1)}{(1 + c + 6\xi)^2} - \frac{\dot{\rho}_1^2(kc\eta - 2\xi)(kc\eta - c - 8\xi - 1)}{\rho_1(1 + c + 6\xi)^2} - 2kg\rho_1\xi + \frac{kc\dot{\eta}\dot{\rho}_2(2kc\eta - c + 2\xi - 1)}{(1 + c - 6\xi)^2} + \frac{\dot{\rho}_2^2(kc\eta - 2\xi)(kc\eta + c - 8\xi + 1)}{\rho_2(1 + c - 6\xi)^2} + 2kg\rho_2\xi + \frac{\ddot{\rho}_1(2\xi - kc\eta)}{1 + c + 6\xi} + \frac{\ddot{\rho}_2(2\xi - kc\eta)}{1 + c - 6\xi}. \tag{2.14}$$

There are three unknowns, $c(t)$, $\xi(t)$ and $\eta(t)$, in (2.7). To close the model, two additional relations will be introduced. In the work of Zhang & Guo (2016), the term $c(t)$, introduced as a density-ratio-dependent function, primarily ensures convergence for spike growth while exerting negligible influence on bubble growth. For incompressible fluids, $c(t) = [-6 + o(1)]\xi(t)$, where $o(1)$ denotes higher-order terms that are typically negligible, reducing the approximation to $-6\xi(t)$ (Zhang & Guo (2016)). However, this formulation fails to capture spike behaviour in variable-density flows at high Atwood numbers, where density variations significantly alter the interfacial dynamics. Specifically, $c(t) = -6\xi(t)$ markedly underestimates the experimental spike growth due to its omission of compressibility effects. To address this limitation, we proposed a modified form

$$c(t) = [-6 + \alpha]\xi(t), \tag{2.15}$$

where the dimensionless parameter α accounts for density variation effects. Drawing from Goncharov & Li (2005), α is formulated using the density-related term $\dot{\rho}_i(t)/\rho_i(t)$, which is crucial to finger growth. Since the spike dynamics is dominated by the heavy fluid (density ρ_2), we define α as

$$\alpha = \frac{-\dot{\rho}_2/\rho_2}{\dot{\rho}_1/\rho_1 + \dot{\rho}_2/\rho_2} = \frac{-\dot{\rho}_2\rho_1}{\dot{\rho}_1\rho_2 + \dot{\rho}_2\rho_1}, \tag{2.16}$$

where ρ_1 and ρ_2 correspond to the light and heavy fluid densities for spikes, respectively. Although α is small compared with the leading term (-6), it critically corrects spike growth predictions in variable-density regimes. Note that (2.16) becomes indeterminate $(0/0)$ under three conditions, including $A = 1$ ($\rho_2 = 0,\ \dot{\rho}_2 = 0$), $A = -1$ ($\rho_1 = 0,\ \dot{\rho}_1 = 0$) and $\dot{\rho}_1 = \dot{\rho}_2 = 0$. In these cases, α is explicitly defined as $\alpha = 0$.

In the work of Zhang & Guo (2016), the finger-tip curvature $\xi(t)$ was approximated as a constant, specifically equal to the quasi-steady curvature ξ_{qs}, which is expressed as $\xi_{qs} = -(3 + A)/(12\sqrt{2(1 + A)})$ for both bubbles and spikes under arbitrary density ratios. Although this approximation is reasonable for moderate initial amplitudes, it becomes inadequate for smaller initial amplitudes. For example, in the following experiments, the initial Atwood number is 0.85, resulting in $\xi_{qs} = -0.167$. For a single-mode case with an initial amplitude of 6 mm and a wavelength of 120 mm, the initial finger-tip curvature ξ_0 (defined as $\xi_0 = -k\eta_0/2$, where η_0 denotes the initial finger amplitude) is calculated as -0.157, which is close to $\xi_{qs} = -0.167$. However, when the initial amplitude is reduced to 2 mm while maintaining the same wavelength (120 mm), ξ_0 decreases to -0.052, approximately one third of $\xi_{qs} = -0.167$. In this situation, the theoretical finger growth is found to deviate significantly from the experimental results, indicating that the assumption $\xi_0 = \xi_{qs}$ is inadequate, particularly for smaller initial amplitudes. Therefore, it is essential to examine the evolution of $\xi(t)$ from its initial value ξ_0 to the asymptotic value ξ_{qs}.

To formulate the expression of finger-tip curvature, we define $f(\xi) = \mathrm{d}\xi/\mathrm{d}\eta$. Following the approach of Zhang & Guo (2022), a first-order asymptotic expansion of $f(\xi)$ is performed at $\xi = \xi_{qs}$. This yields

$$f(\xi) = f(\xi_{qs}) + \beta(\xi - \xi_{qs}). \tag{2.17}$$

https://doi.org/10.1017/jfm.2025.10354 Published online by Cambridge University Press

Here, $\beta = f'(\xi_{qs})$ with $f' = \mathrm{d}f/\mathrm{d}\xi$. Since the finger-tip curvature during the quasi-steady stage is insensitive to amplitude growth (Sohn 2004), i.e. $f(\xi_{qs}) = 0$, we have

$$f(\xi) = \beta(\xi - \xi_{qs}). \tag{2.18}$$

Using the two conditions, $\xi_0 = -k\eta_0/2$ and $\xi_{qs} = -(3+A)/(12\sqrt{2(1+A)})$ (Zhang & Guo 2016), the solution to (2.18) can be expressed as

$$\xi(\eta) = \xi_{qs} + \left[\xi_0 - \xi_{qs}\right]e^{\beta(\eta-\eta_0)}, \tag{2.19}$$

where β remains unknown.

To determine β, we summarise key properties of finger curvature from previous studies:

(i) for $A = 1$, the bubble curvature is given by $\xi = (\xi_0 + 1/6)e^{-3k(\eta-\eta_0)} - 1/6$ (Zhang 1998; Goncharov 2002);
(ii) the bubble curvature in the quasi-steady stage is insensitive to the density ratio (Sohn 2004; Zhang & Guo 2022; Liu *et al.* 2023*b*);
(iii) as $A \to -1$, the spike curvature in the quasi-steady stage tends to infinity (Zhang 1998).

Following Zhang & Guo (2016, 2022), β can be expressed as a Laurent series in terms of $\sqrt{1+A}$. Keeping only the three leading terms yields

$$\beta(A) = \frac{h_{-1}}{\sqrt{1+A}} + h_0 + h_1\sqrt{1+A}, \tag{2.20}$$

where h_{-1}, h_0, h_1 are three constant coefficients. For $A = 1$, (2.19) reduces to $\xi = [\xi_0 + 1/6]e^{\beta(\eta-\eta_0)} - 1/6$, which matches the expression for finger curvature given in property (i). By comparing these two expressions, we have

$$\beta(1) = h_{-1}/\sqrt{2} + h_0 + h_1\sqrt{2} = -3k. \tag{2.21}$$

Based on property (ii), ξ_{qs} is approximately constant for $A \in (0, 1]$. Since $\beta(A)$ represents the higher-order derivative of ξ, it is assumed that $\beta(A)$ is a constant. To satisfy (2.20), $h_1 = h_{-1} = 0$. Substituting these values into (2.21) gives $h_0 = -3k$, namely $\beta(A) = -3k$.

Then, the expression for the variable finger-tip curvature under time-dependent acceleration and density is given by

$$\xi(\eta) = -\frac{3+A}{12\sqrt{2(1+A)}} + \left[-\frac{k\eta_0}{2} + \frac{3+A}{12\sqrt{2(1+A)}}\right]e^{-3k(\eta-\eta_0)}, \tag{2.22}$$

which holds for all $A \in (-1, 1]$. Equation (2.22) characterises the dependence of finger curvature on the initial interface conditions (including A, k and η_0), as well as the interrelation between the morphology evolution and growth rate of fingers.

Property (iii) is used to further assess (2.22). As $A \to -1$, the first term on the right-hand side of (2.22) tends to $-\infty$, while the remaining term approaches zero in the quasi-steady stage. Therefore, property (iii) is satisfied.

Through simple mathematical transformations, $\mathrm{d}\xi/\mathrm{d}t$ and $\mathrm{d}^2\xi/\mathrm{d}t^2$ can be expressed respectively as

$$\frac{\mathrm{d}\xi}{\mathrm{d}t} = \frac{\mathrm{d}\xi}{\mathrm{d}\eta}\frac{\mathrm{d}\eta}{\mathrm{d}t}, \quad \frac{\mathrm{d}^2\xi}{\mathrm{d}t^2} = \frac{\mathrm{d}^2\xi}{\mathrm{d}\eta^2}\left(\frac{\mathrm{d}\eta}{\mathrm{d}t}\right)^2 + \frac{\mathrm{d}\xi}{\mathrm{d}\eta}\frac{\mathrm{d}^2\eta}{\mathrm{d}t^2}. \tag{2.23}$$

Neglecting the higher-order terms results in $\mathrm{d}c/\mathrm{d}t = (-6+\alpha)\,\mathrm{d}\xi/\mathrm{d}t$. Substituting the expression of $\mathrm{d}c/\mathrm{d}t$ and (2.23) into (2.7), the finger growth rate ($v = \mathrm{d}\eta/\mathrm{d}t$), governed

https://doi.org/10.1017/jfm.2025.10354 Published online by Cambridge University Press

by time-dependent acceleration and density, can be obtained by solving the following expression:

$$\dot{v} = -\frac{S_2 v^2 + S_3}{S_1}, \tag{2.24}$$

where

$$S_1 = F_1 + F_2 \frac{\mathrm{d}\xi}{\mathrm{d}\eta}, \tag{2.25}$$

$$S_2 = F_2 \frac{\mathrm{d}^2\xi}{\mathrm{d}\eta^2} + F_3 \left[k^2 c^2 + 16 \left(\frac{\mathrm{d}\xi}{\mathrm{d}\eta} \right)^2 \right] + F_4(-6-\alpha) \left(\frac{\mathrm{d}\xi}{\mathrm{d}\eta} \right)^2, \tag{2.26}$$

$$S_3 = [F_5 + F_6(-6-\alpha)] \frac{\mathrm{d}\xi}{\mathrm{d}\eta} v + F_7. \tag{2.27}$$

We comment that the result of (2.24) is valid for arbitrary density ratios. It should be emphasised that the setting of $A > 0$ and $g > 0$ in (2.24) results in the solution for bubbles, while $A < 0$ and $g < 0$ correspond to the solution for spikes. The rarefaction-induced acceleration and density, required as inputs for (2.24), were recently derived by Gao *et al.* (2024), and their expressions are provided in Appendix A. The density expressions, (A2) and (A3), represent the densities in the vicinity of the interface and incorporate both temporal and spatial (interface position) variations. Therefore, the present model is capable of addressing the spatio-temporal variation of interface density in rarefaction-driven RTI. When $\dot{\rho}_i$ vanishes and both g and ξ are constant, the model (2.24) naturally reduces to the model proposed by Zhang & Guo (2016), which applies to constant acceleration and density conditions. Furthermore, when $\dot{\rho}_i = 0$, $c = 1$ and g is constant, (2.24) recovers to the classical Layzer-type model (Zhang 1998), which is applicable for infinite density ratio extremes ($A = \pm 1$).

To sum up, the contributions of the present model to the theoretical modelling of RTI flows are threefold. First, the effect of time-dependent density on finger evolution, which has seldom been considered in RTI flows, is quantified. Second, the present model can describe the growth behaviours of both bubbles and spikes in rarefaction-driven RTI flows, while the previous model was formulated only for bubbles (Mikaelian 2009). Third, the present model provides the expression for the time-dependent curvature of the finger tip as it evolves from its initial value to the quasi-steady value, in contrast to the previous model that assumed a constant finger-tip curvature (Zhang & Guo 2016). To verify the present model, the experiments and numerical simulations are performed in the following sections.

3. Experimental methods

The experiments of rarefaction-driven RTI are conducted in a horizontal rarefaction tube, as depicted in figure 1(*a*). This tube, with an inner cross-sectional area of 6 mm × 120 mm, contains four main sections: a 1.0 m vacuum section, a 0.35 m transition section, a 0.45 m test section and a 1.0 m reflection section. Both the vacuum and reflection sections are sufficiently long to ensure that the interface evolution during the experimental duration is not affected by the reflected waves from the ends of the tube. Before the experiments, a 3 μm-thick polyethylene terephthalate (PET) diaphragm, secured by a clamp device, is used to separate the vacuum and transition sections. As shown in figure 1(*b*), the clamp consists of two parts, with the left part featuring a sharp blade-like edge. Air is then extracted from the vacuum section using a vacuum pump.

https://doi.org/10.1017/jfm.2025.10354 Published online by Cambridge University Press

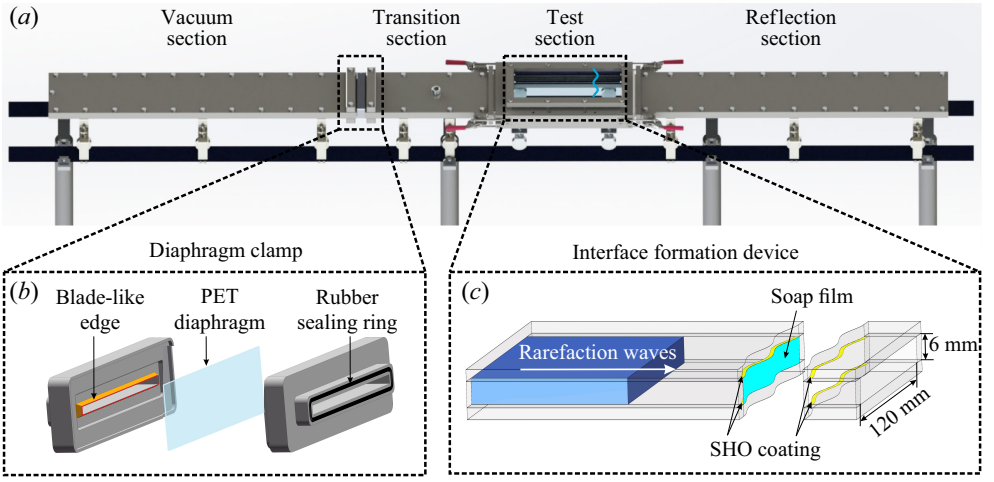


Figure 1. Schematics of the experimental apparatus: the horizontal rarefaction tube (a), the clamp device used to secure the diaphragm (b) and the interface formation device (c). Here, SHO coating denotes the super-hydrophobic-oleophobic coating, used to confine the soap film to the designed shape.

Case	a_0 (mm)	λ (mm)	a_0/λ
2-40	2	40	0.05
2-60	2	60	0.033
2-120	2	120	0.017
3-60	3	60	0.05
6-120	6	120	0.05

Table 1. Initial experimental interface parameters. Here, a_0 and λ represent the initial amplitude and wavelength of the single-mode interface.

When the pressure inside the vacuum section reduces to the PET diaphragm's endurance limit, the sharp edge of the clamp completely cuts off the PET diaphragm, forming rarefaction waves that travel downstream along the transition section. Further details of the rarefaction-tube flow can be found in Appendix B.

In the experiments, to ensure that the evolving interface remains within the rarefaction region, the rarefaction tail must move upstream along the vacuum section after the diaphragm rupture. According to one-dimensional (1-D) gas dynamics theory (Han & Yin 1993), when the pressure ratio p_2/p_1 (where p_2 and p_1 denote the pressures in the transition and vacuum sections, respectively) exceeds 5.969, the rarefaction tail propagates upstream under the present experimental conditions (see Appendix B for the determination of p_2/p_1). In our experiments, the diaphragm ruptures at 10 kPa, yielding $p_2/p_1 = 10$, which satisfies the theoretical criterion for upstream movement of the rarefaction tail.

Five different sets of single-mode interfaces, with their initial amplitudes (a_0) and wavelengths (λ) listed in table 1, are taken into account to study the evolution of rarefaction-driven RTI. For each case, the initial amplitude–wavelength ratio (a_0/λ) does not exceed 0.05, satisfying the small-perturbation hypothesis. The centre of the initial interface for each case is located at 758.5 mm downstream of the diaphragm. The soap-film technique (Li *et al.* 2023) is adopted to generate the single-mode interfaces. Transparent acrylic plates are used to manufacture the interface formation device.

https://doi.org/10.1017/jfm.2025.10354 Published online by Cambridge University Press

As depicted in figure 1(*c*), this interface device consists of two sub-devices, with their edges pre-carved into sinusoidal shapes. To confine the soap film to the designed shape, a super-hydrophobic-oleophobic coating is applied to the sinusoidal edges of the interface device. Then, by pulling a rectangular brush with moderate soap-film solutions on its borders along the sinusoidal edges, a well-defined soap-film interface is generated.

Combinations of SF_6/air and air/helium gas are commonly used for generating heavy/light interfaces in previous experimental studies (Brouillette & Sturtevant 1989; Jourdan & Houas 2005; Zhai *et al.* 2016; Morgan *et al.* 2018; Guo *et al.* 2022*a*,*b*; Li *et al.* 2024). These two gas combinations yield initial Atwood numbers (A_0) of 0.67 and 0.75, respectively, under pure gas conditions. However, in rarefaction-driven flows, the density on both sides of the interface decreases continuously, causing the SF_6/air or air/helium interface to become progressively indistinct in schlieren imaging during late stages (Gao *et al.* 2024). This poses a significant challenge for experimental measurements. To improve the schlieren imaging in the experiments, a higher initial density ratio is required. In this work, CF_4 and helium are selected. In the experiments, after inserting the interface device with a prepared soap film into the test section, CF_4 and helium are injected into the test section through small holes at the transition and reflection sections, respectively. The soap film effectively impedes gas exchange on both sides of the interface, creating a discontinuous CF_4/helium gaseous interface. The inflation rate and duration are strictly controlled to ensure consistent gas concentrations in each experimental run. The volume fractions of both CF_4 and helium for each run are maintained at approximately 90 %, resulting in $A_0 = 0.85$.

A schlieren system with a high-speed camera (FASTCAM SA5, Photron Limited) is used to visualise the flow field. The frame rate of the camera is 30 000 frames per second and the exposure time is 1 μs. The spatial resolution is 0.416 mm pixel^{-1}. Further details about the schlieren system can be found in the previous work (Guo *et al.* 2022*a*). The ambient pressure and temperature are approximately 101.3 kPa and 293.5 K, respectively.

4. Results and discussion

4.1. *Qualitative results*

The rarefaction-induced interface images for five different cases are displayed in figures 2(*a*)–2(*e*). The time origin is defined as the moment when the rarefaction head arrives at the interface centre. As shown in figure 2(*a*), accelerated by the rarefaction waves, the interface gradually moves upstream. In the early stage, the perturbation exhibits a clear 2-D sinusoidal shape (387 μs), indicating that the initial interface shape is well defined. Subsequently, the symmetry of the interface is disrupted (787 μs), forming large-scale finger structures of bubbles and spikes. As time elapses, the bubbles expand, and the spikes elongate significantly, with vortex pairs rolling up at the spike tip (1987–2387 μs). When the initial amplitude is fixed, increasing the interface wavelength results in slower instability evolution due to reduced baroclinic vorticity deposition from the rarefaction waves, as shown in figures 2(*a*)–2(*c*). In contrast, for a fixed wavelength, increasing the initial amplitude accelerates the instability evolution, as depicted in figure 2(*b*,*d*) and figure 2(*c*,*e*).

Notably, during the breakup of the soap film caused by the rarefaction impact, high-wavenumber perturbations are introduced at the CF_4/helium interface. These small perturbations are initially comparable in scale to the rarefaction-induced atomised soap droplets, typically tens of micrometres in size (Ranjan *et al.* 2009). Therefore, the interfaces appear smooth in the early stages, as illustrated in the first column of figure 2. However,

https://doi.org/10.1017/jfm.2025.10354 Published online by Cambridge University Press

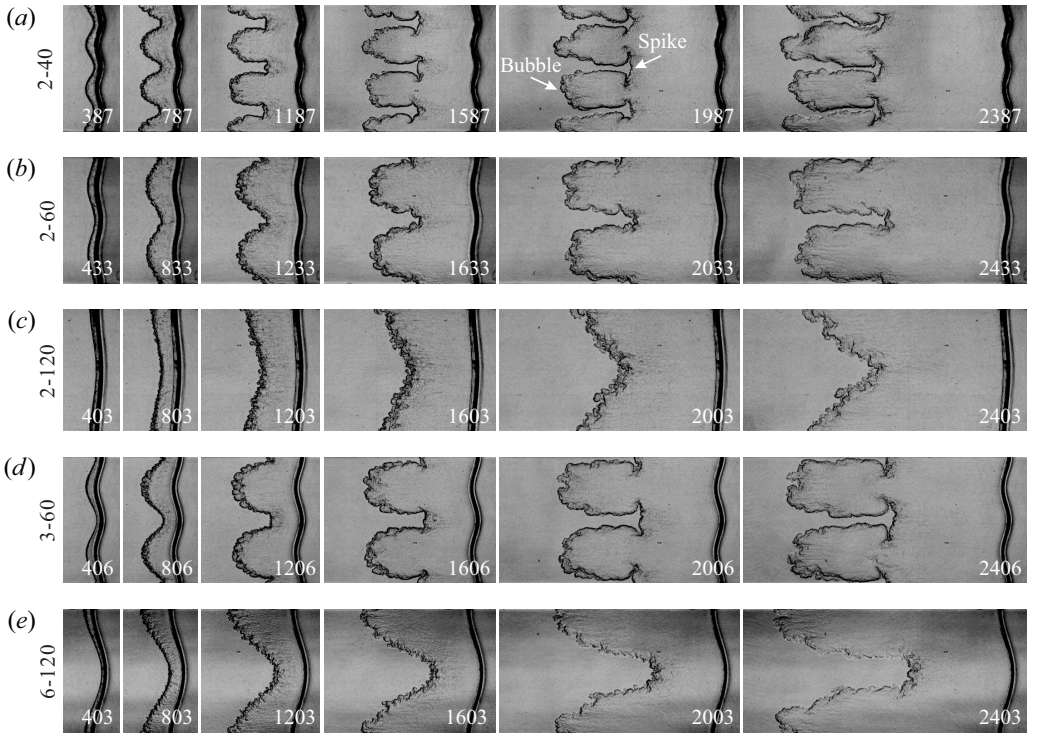


Figure 2. Schlieren images of rarefaction-driven evolution of discontinuous single-mode CF_4/helium interfaces for cases 2-40 (*a*), 2-60 (*b*), 2-120 (*c*), 3-60 (*d*) and 6-120 (*e*). Numbers denote time in μs.

the continuous energy injection from the rarefaction waves results in the sustained development of these small perturbations, triggering secondary RTI. This secondary instability is characterised by the emergence of numerous small vortex structures along the interface, particularly at the bubble tips. Moreover, as the spikes elongate, Kelvin–Helmholtz instabilities develop at the spike stems, generating additional small vortex structures.

4.2. *Quantitative comparisons*

Figure 3(*a–e*) shows the comparisons of finger growth between the theoretical predictions from (2.24) and the experimental results in different cases. The amplitude of bubbles (or spikes) is defined as the distance from the bubble (or spike) tip to the position of a flat interface driven by rarefaction waves, with the flat interface location given by (A5). When secondary RTI develops at the finger tips, the measured position of the bubble (or spike) tip is defined as the average position of small perturbations along the flow direction. Error bars in figure 3(*a–e*) represent the extending range of these perturbations in the flow direction. The black dashed lines in figure 3(*a–e*) indicate the boundary between the linear and nonlinear stages. In the linear stage, spikes and bubbles grow symmetrically with similar exponential growth rates. However, in the nonlinear stage, the growth of both spikes and bubbles gradually approaches an approximately constant rate, with spike growth rates surpassing those of bubbles. The theoretical model (2.24) effectively captures the amplitude growth of spikes and bubbles during both the linear and nonlinear stages.

https://doi.org/10.1017/jfm.2025.10354 Published online by Cambridge University Press

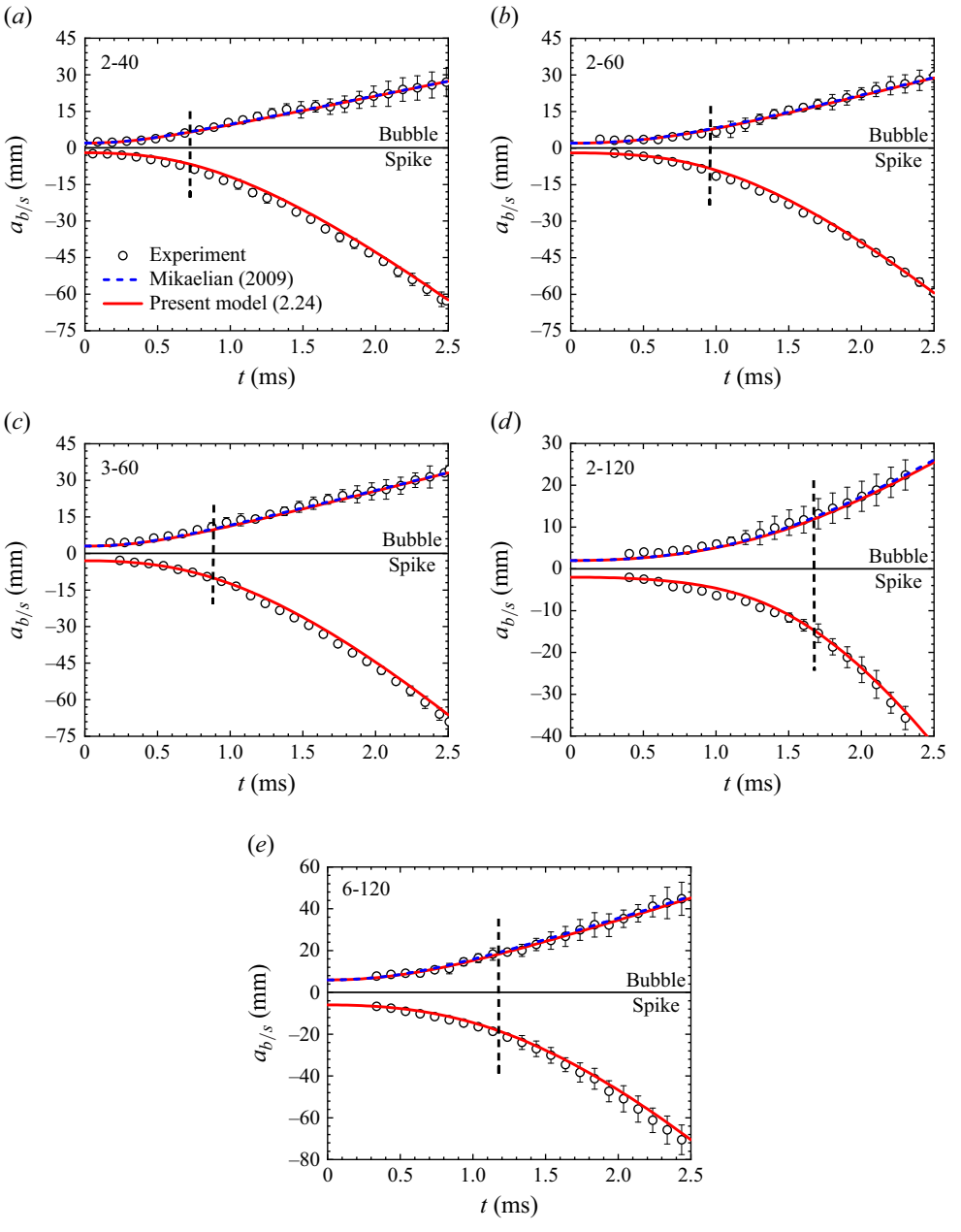


Figure 3. Comparisons of finger growth between the experimental results and the theoretical predictions in different cases. The symbols represent the experimental results. The blue dashed lines represent the theoretical predictions from the model (4.1) and (4.2) of Mikaelian (2009), and the red solid lines represent the theoretical predictions of our model (2.24). The black dashed lines separate the linear stage from the nonlinear stage.

Figure 3(*a–e*) also displays the theoretical curves from the potential-flow model proposed by Mikaelian (2009). The finger amplitude in the Mikaelian model is determined by solving the following two coupled equations:

$$\frac{\mathrm{d}}{\mathrm{d}t}(\rho_1\eta_2) = -\frac{k(k+6\eta_2)}{2}\frac{\mathrm{d}}{\mathrm{d}t}(\rho_1\eta), \tag{4.1}$$

https://doi.org/10.1017/jfm.2025.10354 Published online by Cambridge University Press

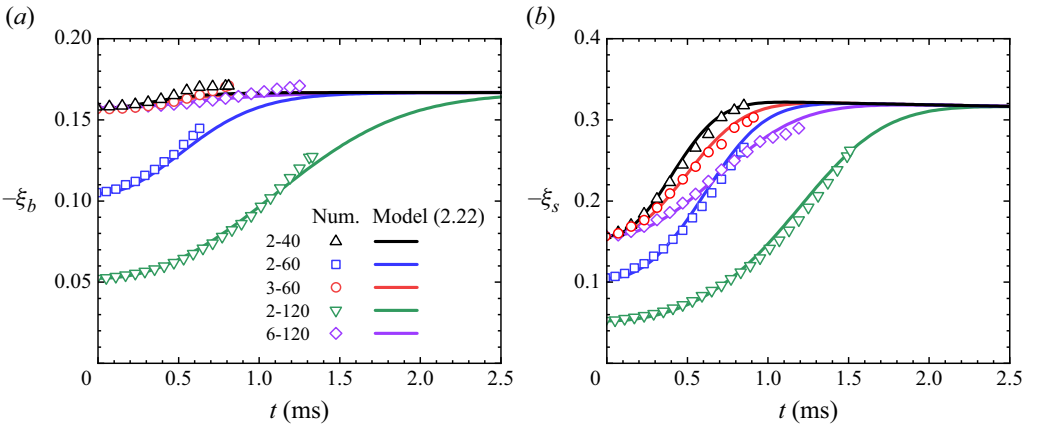


Figure 4. Comparison of curvature for bubbles (a) and spikes (b) between numerical simulations and our model (2.22) in different cases.

$$\rho_1\left\{\frac{k}{2}\frac{\mathrm{d}}{\mathrm{d}t}\left[\frac{1}{\rho_1}\frac{\mathrm{d}}{\mathrm{d}t}(\rho_1\eta)\right]+\frac{k^2}{2}\left[\frac{1}{\rho_1}\frac{\mathrm{d}}{\mathrm{d}t}(\rho_1\eta)\right]^2\right\}+\rho_2\left(\frac{k\dot{b}_1}{2}-\frac{k^2b_1^2}{2}\right)+(\rho_1-\rho_2)(g+\ddot{\eta})\eta_2=0, \tag{4.2}$$

with

$$b_1=\frac{\frac{\mathrm{d}}{\mathrm{d}t}(\rho_2\eta_2)}{k\rho_2(3\eta_2-k/2)}. \tag{4.3}$$

Here, η_2 is related to the finger curvature. Notably, Mikaelian (2009) only provided the theoretical prediction for bubbles; consequently, the theoretical curves for spikes are absent in figure 3(a–e). One can find that the results from the Mikaelian model align closely with those of our model (2.24).

To validate the theoretical temporal evolution of finger curvatures predicted by our model (2.22), we perform numerical simulations initialised with conditions matching experimental cases (see Appendix C for details of the numerical methods). Figures 4(a) and 4(b) compare the simulated curvatures of bubbles (ξ_b) and spikes (ξ_s) against model predictions. Notably, secondary RTI developing along the interface complicates curvature extraction at late times, restricting numerical results to early and intermediate stages. As presented in figure 4(a), for cases with large a_0/λ (2-40, 3-60 and 6-120), the initial bubble curvature is already near its asymptotic value, aligning with the constant-curvature assumption proposed by Zhang & Guo (2016). In contrast, smaller a_0/λ cases exhibit gradual curvature growth, requiring finite time to reach saturation. The spike curvature, as shown in figure 4(b), exhibits analogous behaviour in different cases: the initial value is much smaller than the asymptotic value, but converges to saturation over time. For fixed a_0 (2-40, 2-60 and 2-120), as a_0/λ decreases, the curvature growth for both bubbles and spikes is reduced and the saturation is delayed. A similar trend is observed in cases 2-40, 3-60 and 6-120, which share identical a_0/λ. The dependence of curvature evolution on the initial conditions is effectively described by our model (2.22). Crucially, the saturation timescale of curvature in figure 4 coincides with the linear-to-nonlinear transition observed in amplitude evolution (figure 3). This demonstrates that the model successfully captures the interrelation between the morphology evolution and growth rate of fingers.

https://doi.org/10.1017/jfm.2025.10354 Published online by Cambridge University Press

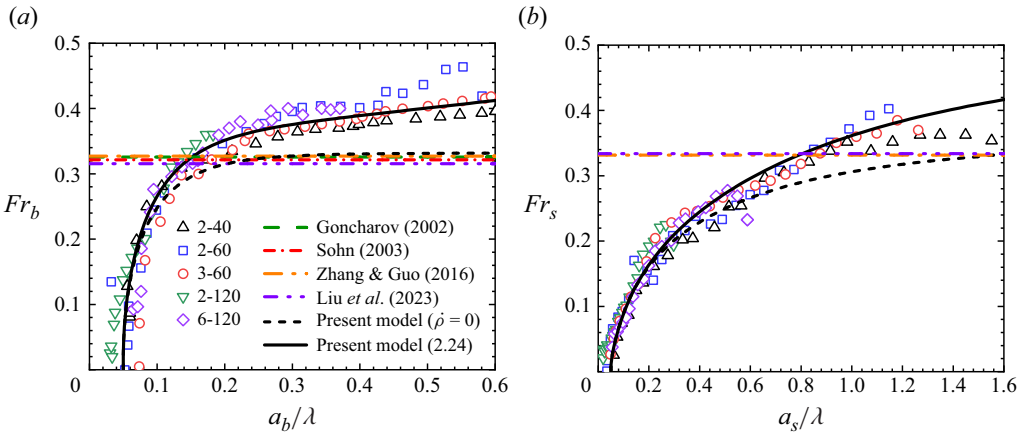


Figure 5. Comparison of Froude numbers for bubbles (Fr_b) and spikes (Fr_s) between experimental results and theoretical predictions. The present model with $\dot{\rho} = 0$ considers variable acceleration only, which is achieved by setting the density derivative terms in (2.12)–(2.14) to zero.

The finger amplitude growth can be scaled using the Froude number, which compares the relative importance of inertial forces to buoyancy forces. The balance between these two forces reveals the nonlinear transition of the instability, where drag counteracts buoyancy forces, leading to a reduction in the acceleration of bubbles and spikes (Morgan *et al.* 2018). According to Ramaprabhu *et al.* (2006), the Froude number (Fr_b and Fr_s) for bubbles and spikes can be expressed as

$$Fr_{b/s} = \frac{U_{b/s}}{\sqrt{Ag\lambda/(1 \pm A)}}, \tag{4.4}$$

where the subscripts 'b' and 's' correspond to bubbles and spikes, respectively; and '$+$' is for bubbles, and '$-$' is for spikes.

Figures 5(a) and 5(b) show the variations of Fr_b and Fr_s versus a_b/λ and a_s/λ, respectively. This scaling approach effectively collapses the growth of bubbles and spikes across different cases. Notably, no obvious re-acceleration occurs within the experimental duration, indicating that the finger growth is still within the quasi-steady stage. Predictions of Fr_b and Fr_s under constant acceleration, obtained from different potential-flow models, are compared with the experimental Froude numbers. The expressions of the quasi-steady velocities ($U_{b/s}^{qs}$) and Froude numbers ($Fr_{b/s}^{qs}$) for bubbles and spikes in different potential-flow models are summarised in table 2. The horizontal lines of Fr_b^{qs} and Fr_s^{qs} given by these potential-flow models are close to each other but consistently lower than the experimental values. This indicates that the rarefaction-driven bubbles and spikes achieve higher asymptotic growth rates compared with constant acceleration conditions. Figures 5(a) and 5(b) also include the theoretical predictions of Fr_b and Fr_s based on our model (2.24), in which the density derivative terms in (2.12)–(2.14) are set to zero. In other words, the model considers variable acceleration only. The predictions are lower than the experimental quasi-steady Froude numbers but approach predictions under constant acceleration. This is consistent with the previous numerical finding that when the flow is driven solely by variable acceleration, the quasi-steady Froude numbers converge to the theoretical values predicted under constant acceleration (Ramaprabhu *et al.* 2016). Therefore, the higher quasi-steady Froude numbers in rarefaction-driven flows are attributed to the compressible effects resulting from time-dependent density, rather than variable acceleration.

https://doi.org/10.1017/jfm.2025.10354 Published online by Cambridge University Press

Model	$U_{b/s}^{qs}$	$Fr_{b/s}^{qs}$
Goncharov (2002)	$\sqrt{\frac{2A}{1+A}\frac{g}{3k}}$	$\sqrt{\frac{1}{3\pi}}$
Sohn (2003)	$\sqrt{\frac{Ag}{(2+A)k}}$	$\sqrt{\frac{1+A}{2\pi(2+A)}}$
Zhang & Guo (2016)	$\sqrt{\frac{8Ag}{3k(1+A)(3+A)}\frac{[3+A+\sqrt{2}(1+A)^{1/2}]^2}{4(3+A)+\sqrt{2}(9+A)(1+A)^{1/2}}}$	$\sqrt{\frac{4}{3\pi(3+A)}\frac{[3+A+\sqrt{2}(1+A)^{1/2}]^2}{4(3+A)+\sqrt{2}(9+A)(1+A)^{1/2}}}$
Liu *et al.* (2023*b*)	$(0.814-0.027A)\sqrt{\frac{Ag}{k(1+A)}}$	$(0.814-0.027A)\sqrt{\frac{1}{2\pi}}$

Table 2. Quasi-steady velocities ($U_{b/s}^{qs}$) and Froude numbers ($Fr_{b/s}^{qs}$) for bubbles and spikes obtained from different potential-flow models. The models of Goncharov (2002) and Sohn (2003) are applicable only to bubbles, whereas the models of Zhang & Guo (2016) and Liu *et al.* (2023*b*) apply to both bubbles and spikes, with $A > 0$ corresponding to bubbles and $A < 0$ to spikes.

To account for the effect of time-dependent density, the finger growth rates obtained by (2.24), along with the acceleration and Atwood numbers in rarefaction-driven flows, are substituted into (4.4), and the time-dependent Fr_b and Fr_s are obtained. From figures 5(*a*) and 5(*b*), the model effectively captures the increase in Froude numbers in rarefaction-driven flows, which demonstrates the significance of the compressibility effect. Note that in the rarefaction field, the density decreases gradually from the wave head to its tail. As the interface moves toward the wave tail, the fluid penetrated by the bubbles and spikes becomes progressively lighter, thereby reducing the drag forces acting on the bubble tips and spike tips. Thus, the bubbles and spikes need to achieve higher asymptotic velocities to balance the drag and buoyancy forces. This results in larger Froude numbers in rarefaction-driven flows, compared with flows driven solely by constant or time-dependent acceleration.

4.3. *Further validation across varied Atwood numbers*

Since the late-time interface profile for lower Atwood number cases becomes increasingly indistinct in experimental schlieren imaging (Gao *et al.* 2024), numerical simulations are employed to assess the model's applicability across different Atwood numbers. In the simulations, four different initial Atwood numbers, $A_0 = 0.23$, 0.50, 0.85 and 0.95, are generated by adjusting the species and concentrations of gases on either side of the interface. The specific gas combinations for these numerical cases are listed in table 3. The initial interface amplitude and wavelength for each numerical case are 2 and 60 mm, respectively. Other initial conditions are the same as those in the experiments. Note that the numerical case with $A_0 = 0.85$ has identical initial conditions compared with the experimental case 2-60.

The comparisons of finger growth at different Atwood numbers between the numerical results and the predictions of our model (2.24) as well as the Mikaelian's model (4.1)–(4.2) are displayed in figure 6(*a–d*). The experimental data for case 2-60 are plotted in figure 6(*c*) for comparison, showing good agreement with the numerical results. For low Atwood numbers ($A_0 = 0.23$), the Mikaelian model slightly overestimates the numerical bubble growth, while for high Atwood numbers ($A_0 = 0.85$ and 0.95), the Mikaelian model gives the same prediction as our model. Overall, our model provides excellent

https://doi.org/10.1017/jfm.2025.10354 Published online by Cambridge University Press

Heavy fluid	Light fluid	A_0
30 % CF_4 + 70 % air	100 % air	0.23
100 % CF_4	100 % air	0.50
90 % CF_4 + 10 % air	90 % He + 10 % air	0.85
100 % SF_6	100 % He	0.95

Table 3. Gas combinations and initial Atwood numbers for the numerical cases.

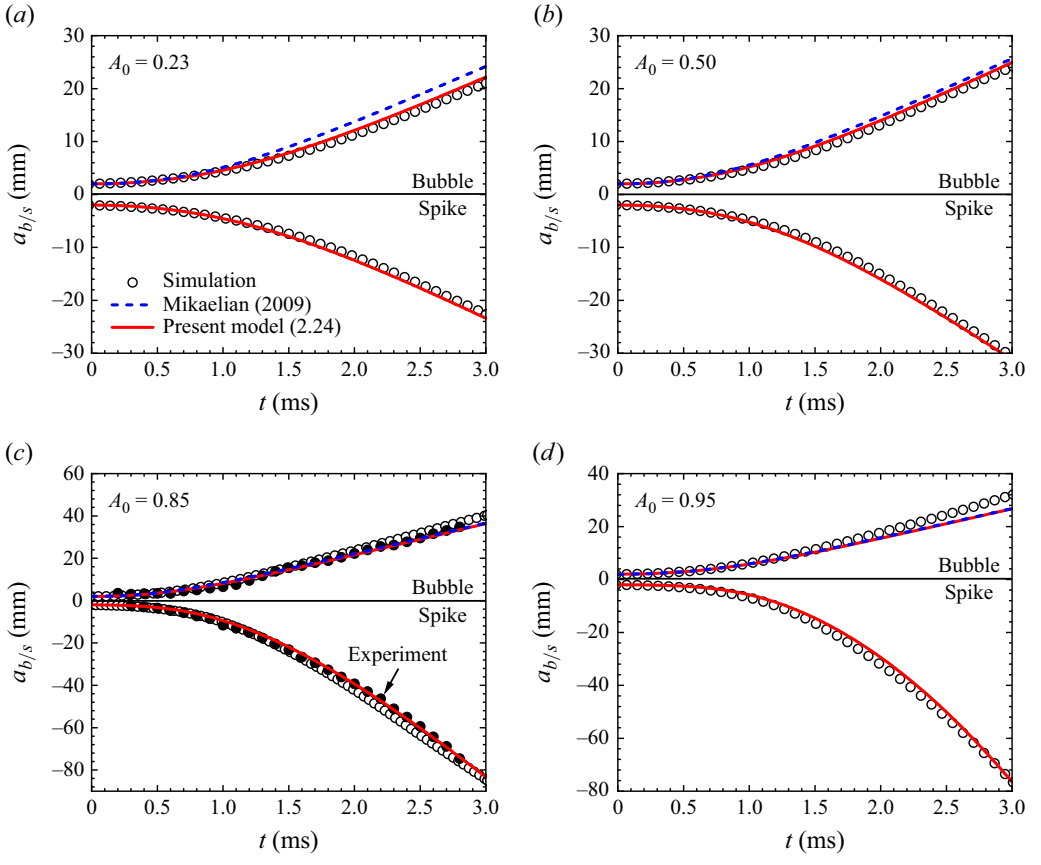


Figure 6. Comparison of amplitude growth for bubbles and spikes between numerical simulations and our model (2.24) at $A_0 = 0.23$ (*a*), 0.50 (*b*), 0.85 (*c*) and 0.95 (*d*). Experimental data of case 2-60 are included in panel (*c*) for comparison.

predictions of the numerical amplitude growth for both bubbles and spikes across different Atwood numbers.

The model (2.24) is also verified through the numerical results for a single-mode SF_6/air interface ($A_0 = 0.67$) obtained from the 2-D Miranda simulations by Morgan *et al.* (2018), as illustrated in figure 7. The comparison demonstrates that our model can also accurately capture the growth of both bubbles and spikes reported by Morgan *et al.* (2018).

Figures 8(*a*) and 8(*b*) compare the temporal evolution of bubble (ξ_b) and spike (ξ_s) curvatures from numerical simulations against prediction of the model (2.22) at varying Atwood numbers (A_0). The bubble curvature evolution shows minimal sensitivity to A_0, with curvature trajectories converging to similar asymptotic values across cases. However,

https://doi.org/10.1017/jfm.2025.10354 Published online by Cambridge University Press

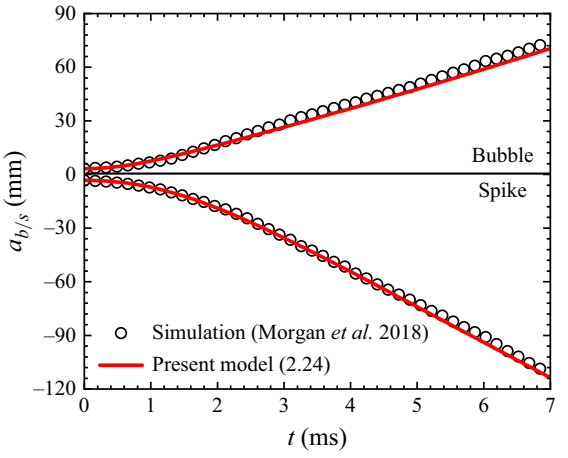


Figure 7. Comparison of finger growth between the theoretical prediction from our model (2.24) and the numerical results of a single-mode SF_6/air interface ($A_0 = 0.67$) from the 2-D Miranda simulations by Morgan *et al.* (2018).

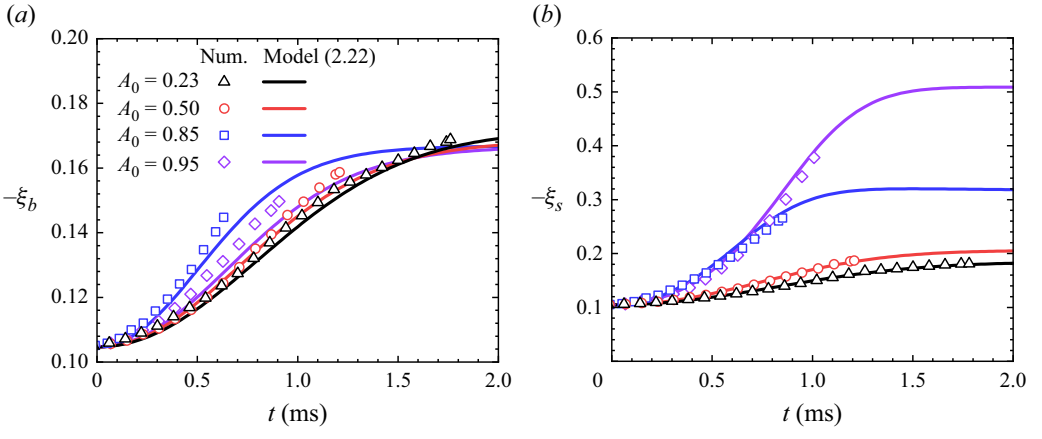


Figure 8. Comparison of curvature for bubbles (a) and spikes (b) between numerical simulations and our model (2.22) at different Atwood numbers.

the spike asymptotic curvature increases with increasing A_0. Notably, during the transition from initial to asymptotic states, the curvature growth rate varies non-monotonically with A_0: the curvature growth rate for $A_0 = 0.85$ exceeds that for $A_0 = 0.95$. This anomaly arises from differences in gas composition (table 3): the $A_0 = 0.85$ case employs a mixture of 90 % CF4/10 % air as heavy fluid, generating stronger rarefaction waves compared with pure SF_6 ($A_0 = 0.95$) (Han & Yin 1993). Enhanced rarefaction amplifies finger growth rates, as shown in figures 6(c) and 6(d), which in turn accelerates curvature evolution. These trends are successfully captured by the model (2.22). In short, the model (2.22) captures both the A_0-dependent asymptotic curvature of spikes and the non-monotonic growth behaviour of bubbles induced by rarefaction effects. This consistency confirms the model's predictive capability across a broad range of A_0.

5. Conclusion

Rayleigh–Taylor instability caused by rarefaction waves not only features variable acceleration but also incorporates time-dependent density, which introduce great

https://doi.org/10.1017/jfm.2025.10354 Published online by Cambridge University Press

challenges in predicting the finger growth behaviours. In this work, by extending Layzer's potential-flow framework (Zhang & Guo 2016) to account for time-dependent acceleration and density, a theoretical model is developed to describe the 2-D amplitude growth of both bubbles and spikes. Relative to the previous models, the present model can evaluate the effect of time-dependent density on the finger growth, and can describe the growth behaviours of both bubbles and spikes in rarefaction-driven RTI flows. In addition, the time-dependent curvature of the finger tip as it evolves from its initial value to the quasi-steady value is quantified.

To validate the model, rarefaction-tube experiments on discontinuous single-mode interfaces with varying amplitude–wavelength combinations generated using the soap-film technique are carried out. In addition, numerical simulations with low, moderate and high Atwood numbers are conducted to further assess the model's applicability across distinct density ratios. The results show that the present model can accurately capture the amplitude growth and curvature evolution of bubbles and spikes across various density ratios. The reliability of our model is also verified by the numerical results obtained from the 2-D Miranda simulations by Morgan *et al.* (2018). Moreover, both the present model and experiments demonstrate that the continuous density reduction in rarefaction-driven flows causes larger asymptotic velocities of bubbles and spikes in the quasi-steady stage, leading to higher Froude numbers relative to those under constant or time-dependent acceleration. This is because the sustained density reduction in the rarefaction field decreases the drag forces acting on the bubble tips and spike tips. As a result, bubbles and spikes achieve larger asymptotic velocities to balance drag and buoyancy forces.

The current model focuses on 2-D, single-mode RTI configurations, however, its framework supports several natural extensions. First, extending the model to 3-D geometries or multi-mode perturbations would enable study of such phenomena as mode coupling and turbulent mixing. Second, the model's input parameters, time-dependent acceleration and density, allow adaptation to arbitrary acceleration profiles and dynamic density evolution. Third, by neglecting density variations, the model simplifies to study RTI dominated by only variable acceleration, such as acceleration reversals (Aslangil, Lawrie & Banerjee 2022; Pak *et al.* 2025).

Acknowledgements. The authors would like to thank Dr Z. Zhou for his help in numerical simulation and analysis.

Funding. This work was supported by the National Natural Science Foundation of China (Nos. 12302371, 12372281 and 12388101), the Youth Innovation Promotion Association CAS, the Strategic Priority Research Program of Chinese Academy of Sciences (No. XDB0620201) and the Fundamental Research Funds for the Central Universities (No. WK2090000048).

Declaration of interests. The authors report no conflict of interest.

Appendix A. Expressions for the rarefaction-induced acceleration and density

Recently, Gao *et al.* (2024) derived the analytical solutions for the rarefaction-induced acceleration (g_r) and the densities (ρ_h and ρ_l) of heavy and light fluids on either side of the interface. The expressions of g_r, ρ_h and ρ_l can be expressed respectively as

$$g_r(t) = \zeta_1\theta_1 t^{\theta_1-1} + \zeta_2\theta_2 t^{\theta_2-1}, \tag{A1}$$

$$\rho_h(t) = \rho_{h0}\left(1+\frac{\gamma_h-1}{2}\frac{u^*}{c_{h0}}\right)^{\frac{2}{\gamma_h-1}}\left(1-\frac{\gamma_h-1}{2}\frac{u_r-u^*}{c^*}\right)^{\frac{2}{\gamma_h-1}}, \tag{A2}$$

$$\rho_l(t) = \rho_{l0}\left(1+\frac{\gamma_l-1}{2}\frac{u_r}{c_{l0}}\right)^{\frac{2}{\gamma_l-1}}, \tag{A3}$$

https://doi.org/10.1017/jfm.2025.10354 Published online by Cambridge University Press

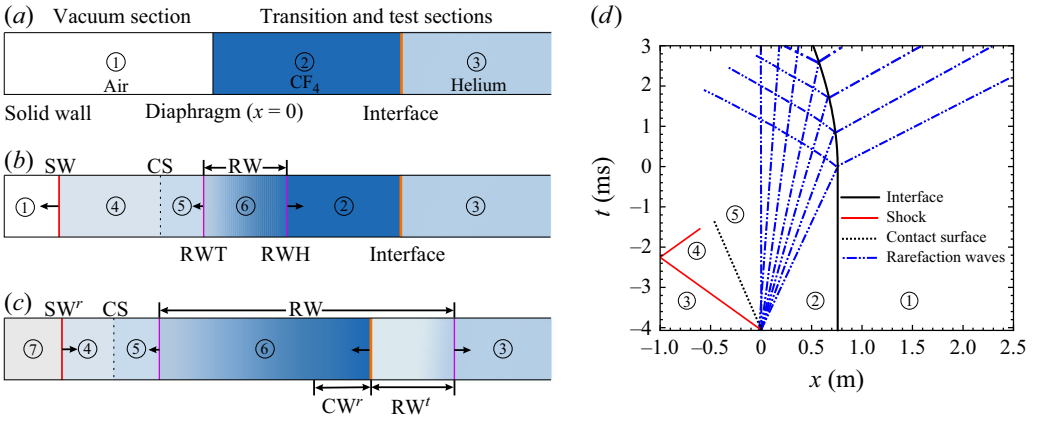


Figure 9. Distributions of flow regions in the rarefaction tube at different moments: (*a*) the moment before the diaphragm rupture, (*b*) the moment after the diaphragm rupture and (*c*) the moment after the rarefaction waves reach the interface. Here, RWH and RWT denote the head and tail of the rarefaction waves, respectively; CS denotes the contact surface; and RW^t and CW^r denote the transmitted rarefaction waves and reflected compression waves, respectively. (*d*) The x–t plot of the 1-D rarefaction-tube flow.

with

$$\theta_{1,2} = \left(-1 \pm \sqrt{1 - \frac{4p_0}{\rho_{l0}} \frac{2\gamma_l(\gamma_l - 1)}{(\gamma_l + 1)^2 c_{l0}^2}} \right) /2. \tag{A4}$$

Here, p_0 denote the initial flow pressure; ρ_{h0} and ρ_{l0} (c_{h0}, c_{l0}; γ_h, γ_l) denote the initial densities (sound speeds and adiabatic indices) for heavy and light fluids, respectively; ζ_1 and ζ_2, dependent on the initial conditions, can be determined by solving geometric relations (see Gao *et al.* 2024); $u^* = (x_r/t - c_{h0})(2/\gamma_h + 1)$ and $c^* = c_{h0} - (\gamma_h - 1/2)u^*$; and x_r and u_r denote the rarefaction-induced interface displacement and velocity, respectively, with

$$x_r(t) = \frac{\zeta_1}{\theta_1 + 1} t^{\theta_1 + 1} + \frac{\zeta_2}{\theta_2 + 1} t^{\theta_2 + 1} - \frac{2}{\gamma - 1} c_{l0} t + \kappa, \tag{A5}$$

and

$$u_r(t) = \zeta_1 t^{\theta_1} + \zeta_2 t^{\theta_2} - \frac{2}{\gamma_l - 1} c_{l0}. \tag{A6}$$

Here, κ in (A5) can be determined by solving geometric relations (Gao *et al.* 2024).

Appendix B. One-dimensional rarefaction-tube flow

Figure 9(*a–c*) presents the distributions of flow regions at specific moments in the rarefaction tube. Before the diaphragm rupture, the diaphragm and the CF_4/helium interface divide the flow fields into regions 1, 2 and 3, as shown in figure 9(*a*). The sudden rupture of the diaphragm generates an upstream-travelling shock (SW), downstream-travelling rarefaction waves (RW) and a contact surface (CS) between these two waves, as depicted in figure 9(*b*). The zones on either side of CS are designated as regions 4 and 5, with both velocities and pressures remaining constant across CS. The RW propagate downstream, transforming region 2 to region 6, characterised by time-dependent flow parameters. The interaction of RW with the CF_4/helium interface generates downstream-moving transmitted rarefaction waves (RW^t) and upstream-moving reflected compression

https://doi.org/10.1017/jfm.2025.10354 Published online by Cambridge University Press

waves (CW^r), leading to the interface moving upstream continuously, as depicted in figure 9(*c*). Figure 9(*d*) shows the x–t diagram of the 1-D rarefaction-tube flow based on our experimental conditions. After the rarefaction waves impact, the interface undergoes variable acceleration motion. During the experimental duration ($t \approx 0$–3 ms), the shock reflected from the end wall does not arrive at the interface, thereby having no influence on the interface evolution.

In the experiments, the evolving interface must remain within the rarefaction region. This requires the rarefaction tail to move upstream along the vacuum section after the diaphragm rupture. The condition for the rarefaction tail moving upstream can be expressed as

$$v_{tl} = c_5 - u_5 < 0, \tag{B1}$$

where v_{tl} denotes the velocity of the rarefaction tail, and c_5 and u_5 denote the sound speed and flow velocity in region 5, respectively. According to 1-D gas dynamics theory (Han & Yin 1993), c_5 and u_5 can be expressed respectively as

$$c_5 = \sqrt{\frac{\gamma_5 p_5}{\rho_5}} = \sqrt{\frac{\gamma_2 p_2}{\rho_2^*}\left\{1 + \frac{\gamma_2 - 1}{2}\left[\sqrt{\frac{\gamma_2 \rho_1^*}{\gamma_1 \rho_2^*}}\frac{M_s(\gamma_1 + 1)}{2(M_s^2 - 1)} - \frac{\gamma_2 - 1}{2}\right]^{-1}\right\}^{\gamma_2}}, \tag{B2}$$

$$u_5 = \frac{2c_1}{\gamma_1 + 1}\left(M_s - \frac{1}{M_s}\right), \tag{B3}$$

where γ, p and ρ (or ρ^*) denote the adiabatic index, pressure and density, respectively, with the subscripts corresponding to the regions illustrated in figure 9; and M_s denotes the shock Mach number, which can be obtained by numerically solving the following expression:

$$\frac{p_2}{p_1} = \left[1 + \frac{2\gamma_1}{\gamma_1 + 1}(M_s^2 - 1)\right]\left[1 - \frac{\gamma_2 - 1}{\gamma_1 + 1}\frac{c_1}{c_2}\left(M_s - \frac{1}{M_s}\right)\right]^{-\frac{2\gamma_2}{\gamma_2 - 1}}, \tag{B4}$$

with p_2/p_1 denoting the initial pressure ratio of gases on either side of the diaphragm. Combining (B1)–(B4), v_{tl} can be expressed as a function of p_2/p_1. By numerically solving the relation between v_{tl} and p_2/p_1, the condition for $v_{tl} < 0$ is determined as $p_2/p_1 > 5.969$. In our experiments, the diaphragm is broken at 10 kPa, resulting in $p_2/p_1 = 10$, ensuring that the rarefaction tail consistently moves upstream.

Appendix C. Numerical methods

The rarefaction–interface interactions are simulated by solving 2-D compressible multi-component Euler equations. The optimised six-point weighted compact nonlinear scheme (WCNS) with minimum dispersion and adaptive dissipation (Zhou *et al.* 2023*b*) is used. Combined with the double-flux algorithm of Abgrall & Karni (2001), the optimised WCNS scheme is extended to multi-species flows, demonstrating a good capability in simulating RTI and shock-induced interface instabilities (Zhou *et al.* 2023*a*, *b*, 2024).

The schematic of the computational domain is presented in figure 10(*a*), where the virtual diaphragm is located at $x = 0$, the initial interface at $x = 758.5$ mm and the left and right boundaries of the domain at $x = -700$ and 1400 mm, respectively. The domain length is sufficiently large to prevent interference from reflected waves produced at the domain boundaries during the simulation. A pressure difference is initially applied across $x = 0$, forming rarefaction waves that propagate in the positive direction along the x-axis.

https://doi.org/10.1017/jfm.2025.10354 Published online by Cambridge University Press

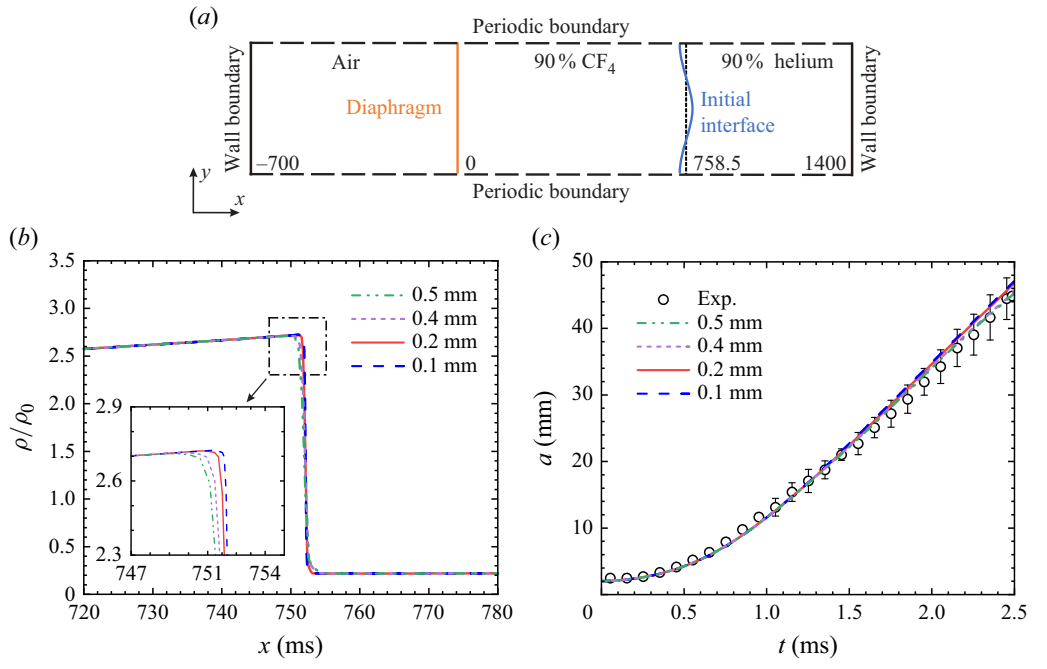


Figure 10. (*a*) The computational domain used for the rarefaction–interface interaction. Numerical results of case 2–40 under different mesh sizes: (*b*) density distribution along the symmetric line of the interface at $t = 911$ μs, and (*c*) temporal variations of the perturbation amplitude. Experimental data of case 2-40 are included in panel (*c*) for comparison.

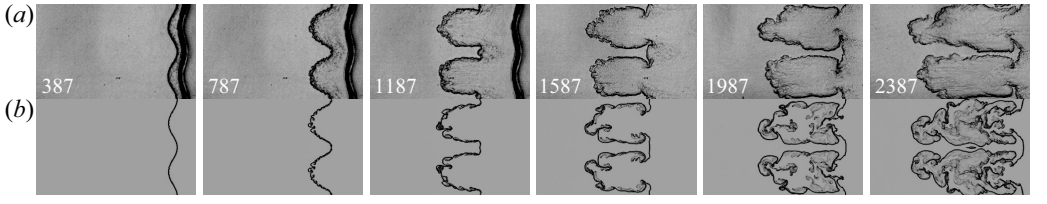


Figure 11. Comparison between the experimental (*a*) and numerical (*b*) schlieren images of interface evolution for a single-mode CF_4/helium interface in case 2-40. Numbers denote time in μs.

Four mesh sizes of 0.5, 0.4, 0.2 and 0.1 mm are adopted for grid convergence examination. The initial conditions for the numerical simulations match those of the experimental case 2-40. Figure 10(*b*) shows the density distribution along the symmetry line of the interface at $t = 911$ μs, and figure 10(*c*) shows the temporal variations of the perturbation amplitude. As the grid size decreases, both the density and amplitude curves converge, with similar results for mesh sizes of 0.2 and 0.1 mm. To balance computational cost and accuracy, a mesh size of 0.2 mm is selected in computations.

The interface evolution in case 2-40 is compared between experimental and numerical results, as shown in figure 11. To maintain a discontinuous interface, a diffusion thickness of 0.5 mm is used in the simulations. This sharp interface introduces numerous small perturbations due to the Cartesian gridding. These small perturbations grow continuously under sustained energy injection from the rarefaction waves, triggering secondary RTI, as illustrated in figure 11(*b*). Although the origins of the small perturbations differ between the simulation and the experiment, the interface evolution morphologies in

https://doi.org/10.1017/jfm.2025.10354 Published online by Cambridge University Press

figures 11(*a*) and 11(*b*) exhibit strong similarity. A quantitative comparison between the experimental and numerical results is presented in figure 10(*c*), demonstrating good agreement.

References

Abarzhi, S.I. 2003 Rayleigh–Taylor and Richtmyer–Meshkov instabilities for fluids with a finite density ratio. *Phys. Lett. A* **317** (5–6), 470–476.

Abgrall, R. & Karni, S. 2001 Computations of compressible multifluids. *J. Comput. Phys.* **169** (2), 594–623.

Aglitskiy, Y. *et al.* 2010 Basic hydrodynamics of Richtmyer–Meshkov-type growth and oscillations in the inertial confinement fusion-relevant conditions. *Phil. Trans. R. Soc. A* **368** (1916), 1739–1768.

Akula, B., Suchandra, P., Mikhaeil, M. & Ranjan, D. 2017 Dynamics of unstably stratified free shear flows: an experimental investigation of coupled Kelvin–Helmholtz and Rayleigh–Taylor instability. *J. Fluid Mech.* **816**, 619–660.

Alon, U., Hecht, J., Ofer, D. & Shvarts, D. 1995 Power laws and similarity of Rayleigh–Taylor and Richtmyer–Meshkov mixing fronts. *Phys. Rev. Lett.* **74** (4), 534–537.

Andrews, M.J. & Dalziel, S.B. 2010 Small Atwood number Rayleigh–Taylor experiments. *Phil. Trans. R. Soc. A* **368** (1916), 1663–1679.

Aslangil, D., Lawrie, A.G.W. & Banerjee, A. 2022 Effects of variable deceleration periods on Rayleigh–Taylor instability with acceleration reversals. *Phys. Rev. E.* **105** (6), 065103.

Banerjee, A. & Andrews, M.J. 2006 Statistically steady measurements of Rayleigh–Taylor mixing in a gas channel. *Phys. Fluids* **18** (3), 035107.

Banerjee, A., Kraft, W.N. & Andrews, M.J. 2010 Detailed measurements of a Rayleigh–Taylor mixing layer from small to intermediate Atwood numbers. *J. Fluid Mech.* **659**, 127–190.

Bian, X., Aluie, H., Zhao, D., Zhang, H. & Livescu, D. 2020 Revisiting the late-time growth of single-mode Rayleigh–Taylor instability and the role of vorticity. *Physica D* **403**, 132250.

Brouillette, M. & Sturtevant, B. 1989 Growth induced by multiple shock waves normally incident on plane gaseous interfaces. *Physica D* **37** (1–3), 248–263.

Brouillette, M. & Sturtevant, B. 1994 Experiments on the Richtmyer–Meshkov instability: single-scale perturbations on a continuous interface. *J. Fluid Mech.* **263**, 271–292.

Cabot, W.H. & Cook, A.W. 2006 Reynolds number effects on Rayleigh–Taylor instability with possible implications for type Ia supernovae. *Nat. Phys.* **2** (8), 562–568.

Dimonte, G. *et al.* 1996 A linear electric motor to study turbulent hydrodynamics. *Rev. Sci. Instrum.* **67** (1), 302–306.

Dimonte, G. & Schneider, M. 2000 Density ratio dependence of Rayleigh–Taylor mixing for sustained and impulsive acceleration histories. *Phys. Fluids* **12** (2), 304–321.

Dimonte, G. *et al.* 2004 A comparative study of the turbulent Rayleigh–Taylor instability using high-resolution three-dimensional numerical simulations: the Alpha-Group collaboration. *Phys. Fluids* **16** (5), 1668–1693.

Duff, R.E., Harlow, F.H. & Hirt, C.W. 1962 Effects of diffusion on interface instability between gases. *Phys. Fluids* **5** (4), 417–425.

Fu, C., Zhao, Z., Wang, P., Liu, N., Wan, Z. & Lu, X. 2023 Bubble re-acceleration behaviours in compressible Rayleigh–Taylor instability with isothermal stratification. *J. Fluid Mech.* **954**, A16.

Gao, X., Guo, X., Zhai, Z. & Luo, X. 2024 Interfacial instabilities driven by co-directional rarefaction and shock waves. *J. Fluid Mech.* **980**, A20.

Goncharov, V.N. 2002 Analytical model of nonlinear, single-mode, classical Rayleigh–Taylor instability at arbitrary Atwood numbers. *Phys. Rev. Lett.* **88** (13), 134502.

Goncharov, V.N. & Li, D. 2005 Effects of temporal density variation and convergent geometry on nonlinear bubble evolution in classical Rayleigh–Taylor instability. *Phys. Rev. E.* **71** (4), 046306.

Goncharov, V.N., Skupsky, S., Boehly, T.R., Knauer, J.P., McKenty, P., Smalyuk, V.A., Town, R.P.J., Gotchev, O.V., Betti, R. & Meyerhofer, D.D. 2000 A model of laser imprinting. *Phys. Plasmas* **7** (5), 2062–2068.

Guo, W. & Zhang, Q. 2020 Universality and scaling laws among fingers at Rayleigh–Taylor and Richtmyer–Meshkov unstable interfaces in different dimensions. *Physica D* **403**, 132304.

Guo, X., Cong, Z., Si, T. & Luo, X. 2022*a* Shock-tube studies of single- and quasi-single-mode perturbation growth in Richtmyer–Meshkov flows with reshock. *J. Fluid Mech.* **941**, A65.

Guo, X., Si, T., Zhai, Z. & Luo, X. 2022*b* Large-amplitude effects on interface perturbation growth in Richtmyer–Meshkov flows with reshock. *Phys. Fluids* **34** (8), 082118.

https://doi.org/10.1017/jfm.2025.10354 Published online by Cambridge University Press

HAN, Z. & YIN, X. 1993 *Shock Dynamics*. Kluwer Academic Publishers and Science Press.
HECHT, J., ALON, U. & SHVARTS, D. 1994 Potential flow models of Rayleigh–Taylor and Richtmyer–Meshkov bubble fronts. *Phys. Fluids* **6** (12), 4019–4030.
HUANG, Z., DE LUCA, A., ATHERTON, T.J., BIRD, M., ROSENBLATT, C. & CARLES, P. 2007 Rayleigh–Taylor instability experiments with precise and arbitrary control of the initial interface shape. *Phys. Rev. Lett.* **99** (20), 204502.
JACOBS, J.W. & DALZIEL, S.B. 2005 Rayleigh–Taylor instability in complex stratifications. *J. Fluid Mech.* **542**, 251–279.
JOURDAN, G. & HOUAS, L. 2005 High-amplitude single-mode perturbation evolution at the Richtmyer–Meshkov instability. *Phys. Rev. Lett.* **95** (20), 204502.
KUCHERENKO, Y.A., BALABIN, S.I., ARDASHOVA, R.I., KOZELKOV, O.E., DULOV, A.V. & ROMANOV, I.A. 2003 Experimental study of the influence of the stabilizing properties of transitional layers on the turbulent mixing evolution. *Laser Particle Beams* **21** (3), 369–373.
KUCHERENKO, Y.A., BALABIN, S.I., CHERRET, R. & HAAS, J.F. 1997 Experimental investigation into inertial properties of Rayleigh–Taylor turbulence. *Laser Particle Beams* **15** (1), 25–31.
LAWRIE, A.G.W. & DALZIEL, S.B. 2011 Rayleigh–Taylor mixing in an otherwise stable stratification. *J. Fluid Mech.* **688**, 507–527.
LAYZER, D. 1955 On the instability of superposed fluids in a gravitational field. *Astrophys. J.* **122**, 1–12.
LEWIS, D.J. 1950 The instability of liquid surfaces when accelerated in a direction perpendicular to their planes. II. *Proc. R. Soc. Lond. A* **202** (1068), 81–96.
LI, C. & BOOK, D.L. 1991 Instability generated by acceleration due to rarefaction waves. *Phys. Rev. A* **43** (6), 3153–3156.
LI, C., KAILASANATH, K. & BOOK, D.L. 1991 Mixing enhancement by expansion waves in supersonic flows of different densities. *Phys. Fluids* **3** (5), 1369–1373.
LI, J., CAO, Q., WANG, H., ZHAI, Z. & LUO, X. 2023 New interface formation method for shock–interface interaction studies. *Exp. Fluids* **64** (11), 170.
LI, J., CHEN, C., ZHAI, Z. & LUO, X. 2024 Effects of compressibility on Richtmyer–Meshkov instability of heavy/light interface. *Phys. Fluids* **36** (5), 056104.
LIANG, Y., ALKINDI, A., ALZEYOUDI, K., LIU, L., ALI, M. & MASMOUDI, N. 2024 Experimental investigation of three-dimensional Rayleigh–Taylor instability of a gaseous interface. *J. Fluid Mech.* **994**, A7.
LIANG, Y., ZHAI, Z., LUO, X. & WEN, C. 2020 Interfacial instability at a heavy/light interface induced by rarefaction waves. *J. Fluid Mech.* **885**, A42.
LINDEN, P.F., REDONDO, J.M. & YOUNGS, D.L. 1994 Molecular mixing in Rayleigh–Taylor instability. *J. Fluid Mech.* **265**, 97–124.
LIU, C., WU-WANG, H., ZHANG, Y. & XIAO, Z. 2023*a* A decoupled mechanism of interface growth in single-mode hydrodynamic instabilities. *J. Fluid Mech.* **964**, A37.
LIU, C., ZHANG, Y. & XIAO, Z. 2023*b* A unified theoretical model for spatiotemporal development of Rayleigh–Taylor and Richtmyer–Meshkov fingers. *J. Fluid Mech.* **954**, A13.
MIKAELIAN, K.O. 1998 Analytic approach to nonlinear Rayleigh–Taylor and Richtmyer–Meshkov instabilities. *Phys. Rev. Lett.* **80** (3), 508–511.
MIKAELIAN, K.O. 2008 Limitations and failures of the Layzer model for hydrodynamic instabilities. *Phys. Rev. E.* **78** (1), 015303.
MIKAELIAN, K.O. 2009 Reshocks, rarefactions, and the generalized Layzer model for hydrodynamic instabilities. *Phys. Fluids* **21** (2), 024103.
MIKAELIAN, K.O. 2014 Shock-induced interface instability in viscous fluids and metals. *Phys. Rev. E.* **89** (5), 053009.
MORGAN, R.V., CABOT, W.H., GREENOUGH, J.A. & JACOBS, J.W. 2018 Rarefaction-driven Rayleigh–Taylor instability. Part 2. Experiments and simulations in the nonlinear regime. *J. Fluid Mech.* **838**, 320–355.
MORGAN, R.V. & JACOBS, J.W. 2020 Experiments and simulations on the turbulent, rarefaction wave driven Rayleigh–Taylor instability. *J. Fluids Engng* **142** (12), 121101.
MORGAN, R.V., LIKHACHEV, O.A. & JACOBS, J.W. 2016 Rarefaction-driven Rayleigh–Taylor instability. Part 1. Diffuse-interface linear stability measurements and theory. *J. Fluid Mech.* **791**, 34–60.
MOTL, B., OAKLEY, J., RANJAN, D., WEBER, C., ANDERSON, M. & BONAZZA, R. 2009 Experimental validation of a Richtmyer–Meshkov scaling law over large density ratio and shock strength ranges. *Phys. Fluids* **21** (12), 126102.
PACITTO, G., FLAMENT, C., BACRI, J.C. & WIDOM, M. 2000 Rayleigh–Taylor instability with magnetic fluids: experiment and theory. *Phys. Rev. E.* **62** (6), 7941–7948.

https://doi.org/10.1017/jfm.2025.10354 Published online by Cambridge University Press

PAK, N., THERIOT, E., ASLANGIL, D., LAWRIE, A. & BANERJEE, A. 2025 Recovery towards self-similarity in Rayleigh–Taylor instability under stepwise and sinusoidal acceleration reversals. *Phys. Rev. E.* **111** (2), 025107.

QIAO, X. & LAN, K. 2021 Novel target designs to mitigate hydrodynamic instabilities growth in inertial confinement fusion. *Phys. Rev. Lett.* **126** (18), 185001.

RAMAPRABHU, P. & DIMONTE, G. 2005 Single-mode dynamics of the Rayleigh–Taylor instability at any density ratio. *Phys. Rev. E.* **71** (3), 036314.

RAMAPRABHU, P., DIMONTE, G. & ANDREWS, M.J. 2005 A numerical study of the influence of initial perturbations on the turbulent Rayleigh–Taylor instability. *J. Fluid Mech.* **536**, 285–319.

RAMAPRABHU, P., DIMONTE, G., YOUNG, Y., CALDER, A.C. & FRYXELL, B. 2006 Limits of the potential flow approach to the single-mode Rayleigh–Taylor problem. *Phys. Rev. E.* **74** (6), 066308.

RAMAPRABHU, P., KARKHANIS, V., BANERJEE, R., VARSHOCHI, H., KHAN, M. & LAWRIE, A.G.W. 2016 Evolution of the single-mode Rayleigh–Taylor instability under the influence of time-dependent accelerations. *Phys. Rev. E.* **93** (1), 013118.

RANJAN, D., NIEDERHAUS, J.H.J., OAKLEY, J., ANDERSON, M.H. & BONAZZA, R. 2009 Experimental investigation of shock-induced distortion of a light spherical gas inhomogeneity. In *Shock Waves*. pp. 1175–1180, Springer.

RAYLEIGH, L. 1883 Investigation of the character of the equilibrium of an incompressible heavy fluid of variable density. *Proc. Lond. Math. Soc.* **14**, 170–177.

READ, K.I. 1984 Experimental investigation of turbulent mixing by Rayleigh–Taylor instability. *Physica D* **12** (1–3), 45–58.

SNIDER, D.M. & ANDREWS, M.J. 1994 Rayleigh–Taylor and shear driven mixing with an unstable thermal stratification. *Phys. Fluids* **6** (10), 3324–3334.

SOHN, S.I. 2003 Simple potential-flow model of Rayleigh–Taylor and Richtmyer–Meshkov instabilities for all density ratios. *Phys. Rev. E.* **67** (2), 026301.

SOHN, S.I. 2004 Vortex model and simulations for Rayleigh–Taylor and Richtmyer–Meshkov instabilities. *Phys. Rev. E.* **69** (3), 036703.

TAYLOR, G. 1950 The instability of liquid surfaces when accelerated in a direction perpendicular to their planes. I. *Proc. R. Soc. Lond. A. Math. Phys. Sci.* **201** (1065), 192–196.

URZAY, J. 2018 Supersonic combustion in air-breathing propulsion systems for hypersonic flight. *Annu. Rev. Fluid Mech.* **50** (1), 593–627.

WADDELL, J.T., NIEDERHAUS, C.E. & JACOBS, J.W. 2001 Experimental study of Rayleigh–Taylor instability: low Atwood number liquid systems with single-mode initial perturbations. *Phys. Fluids* **13** (5), 1263–1273.

WANG, R., SONG, Y., MA, Z., MA, D., WANG, L. & WANG, P. 2022*a* The transition to turbulence in rarefaction-driven Rayleigh–Taylor mixing: effects of diffuse interface. *Phys. Fluids* **34** (1), 015125.

WANG, R., SONG, Y., MA, Z., ZHANG, C., SHI, X., WANG, L. & WANG, P. 2022*b* Transitional model for rarefaction-driven Rayleigh−Taylor mixing on the diffuse interface. *Phys. Fluids* **34** (7), 075136.

WEI, T. & LIVESCU, D. 2012 Late-time quadratic growth in single-mode Rayleigh–Taylor instability. *Phys. Rev. E.* **86** (4), 046405.

WHITE, J., OAKLEY, J., ANDERSON, M. & BONAZZA, R. 2010 Experimental measurements of the nonlinear Rayleigh–Taylor instability using a magnetorheological fluid. *Phys. Rev. E.* **81** (2), 026303.

WILKINSON, J.P. & JACOBS, J.W. 2007 Experimental study of the single-mode three-dimensional Rayleigh–Taylor instability. *Phys. Fluids* **19** (12), 124102.

YOUNGS, D.L. 1989 Modeling turbulent mixing by Rayleigh–Taylor instability. *Physica D* **37** (1–3), 270–287.

YOUNGS, D.L. 2013 The density ratio dependence of self-similar Rayleigh–Taylor mixing. *Phil. Trans. R. Soc. A* **371** (2003), 20120173.

ZHAI, Z., DONG, P., SI, T. & LUO, X. 2016 The Richtmyer–Meshkov instability of a 'V' shaped air/helium interface subjected to a weak shock. *Phys. Fluids* **28** (8), 082104.

ZHANG, Q. 1998 Analytical solutions of Layzer-type approach to unstable interfacial fluid mixing. *Phys. Rev. Lett.* **81** (16), 3391–3394.

ZHANG, Q. & GUO, W. 2016 Universality of finger growth in two-dimensional Rayleigh–Taylor and Richtmyer–Meshkov instabilities with all density ratios. *J. Fluid Mech.* **786**, 47–61.

ZHANG, Q. & GUO, W. 2022 Quantitative theory for spikes and bubbles in the Richtmyer–Meshkov instability at arbitrary density ratios. *Phys. Rev. Fluids* **7** (9), 093904.

ZHOU, Y. 2017*a* Rayleigh–Taylor and Richtmyer–Meshkov instability induced flow, turbulence, and mixing. I. *Phys. Rep.* **720-722**, 1–136.

ZHOU, Y. 2017*b* Rayleigh–Taylor and Richtmyer–Meshkov instability induced flow, turbulence, and mixing. II. *Phys. Rep.* **723–725**, 1–160.

https://doi.org/10.1017/jfm.2025.10354 Published online by Cambridge University Press

ZHOU, Y., CLARK, T.T., CLARK, D.S., GLENDINNING, S.G., SKINNER, M.A., HUNTINGTON, C.M., HURRICANE, O.A., DIMITS, A.M. & REMINGTON, B.A. 2019 Turbulent mixing and transition criteria of flows induced by hydrodynamic instabilities. *Phys. Plasmas* **26** (8), 080901.

ZHOU, Y., SADLER, J.D. & HURRICANE, O.A. 2025 Instabilities and mixing in inertial confinement fusion. *Annu. Rev. Fluid Mech.* **57** (1), 197–225.

ZHOU, Y. *et al.* 2021 Rayleigh–Taylor and Richtmyer–Meshkov instabilities: a journey through scales. *Physica D* **423**, 132838.

ZHOU, Z., DING, J. & CHENG, W. 2024 Mixing and inter-scale energy transfer in Richtmyer–Meshkov turbulence. *J. Fluid Mech.* **984**, A56.

ZHOU, Z., DING, J., CHENG, W. & LUO, X. 2023*a* Scaling law of structure function of Richtmyer–Meshkov turbulence. *J. Fluid Mech.* **972**, A18.

ZHOU, Z., DING, J., HUANG, S. & LUO, X. 2023*b* A new type of weighted compact nonlinear scheme with minimum dispersion and adaptive dissipation for compressible flows. *Comput. Fluids* **262**, 105934.

ZHOU, Z., ZHANG, Y. & TIAN, B. 2018 Dynamic evolution of Rayleigh–Taylor bubbles from sinusoidal, W-shaped, and random perturbations. *Phys. Rev. E.* **97** (3), 033108.

https://doi.org/10.1017/jfm.2025.10354 Published online by Cambridge University Press